A Solution-Adaptive Upwind Scheme for Ideal Magnetohydrodynamics

Kenneth G. Powell,* Philip L. Roe,* Timur J. Linde,* Tamas I. Gombosi,†
and Darren L. De Zeeuw†

*W. M. Keck Foundation CFD Laboratory, Department of Aerospace Engineering, University of Michigan,
Ann Arbor, Michigan 48109-2140; and †Space Physics Research Laboratory, Department of Atmospheric,
Oceanic and Space Sciences, University of Michigan, Ann Arbor, Michigan 48109-2143
E-mail: {powell, philroe, linde, tamas, darrens}@umich.edu

This paper presents a computational scheme for compressible magnetohydrody-
namics (MHD). The scheme is based on the same elements that make up many
modern compressible gas dynamics codes: a high-resolution upwinding based on
an approximate Riemann solver for MHD and limited reconstruction; an optimally
smoothing multi-stage time-stepping scheme; and solution-adaptive refinement and
coarsening. In addition, a method for increasing the accuracy of the scheme by sub-
tracting off an embedded steady magnetic field is presented. Each of the pieces of
the scheme is described, and the scheme is validated and its accuracy assessed by
comparison with exact solutions. Results are presented for two three-dimensional
calculations representative of the interaction of the solar wind with a magenetized
planet. © 1999 Academic Press

1. INTRODUCTION

Many flows, particularly astrophysical flows, are electrically conducting, and the elec-
tromagnetic forces in these flows can be of the same order as, or even greater than, the
hydrodynamic forces. The governing equations of magnetohydrodynamics (MHD) are of-
ten used for conducting flows in which relativistic effects are unimportant and the continuum
assumption is valid. These governing equations, which basically merge the Euler equations
of gas dynamics with the Maxwell equations of electromagnetics, have long been studied
for their elegant yet complicated structure.

Solving the MHD equations computationally entails grappling with a host of issues. The
ideal MHD equations—the limit in which viscous and resistive effects are ignored—have
a wave-like structure analogous to, though substantially more complicated than, that of
the Euler equations of gas dynamics. The ideal MHD equations exhibit degeneracies of a

type that do not arise in gas dynamics and also, as they are normally written, have an added constraint of zero divergence of the magnetic field.

Because astrophysical flows are highly compressible, Godunov-type techniques appear to be an attractive approach for this class of problem. Thus, beginning with the work of Brio and Wu [1] and Zachary and Colella [2], the development of solution techniques for the ideal MHD equations based on approximate Riemann solvers has been studied. In both of those references, a Roe-type scheme for one-dimensional ideal MHD was developed and studied. Roe and Balsara [3] proposed a refinement to the eigenvector normalizations developed in the previous work, and Dai and Woodward [4] developed a nonlinear approximate Riemann solver for MHD. Other approximate Riemann solvers were also developed by Croisille *et al.* [5] (a kinetic scheme) and by Linde [6] (an HLLE-type scheme). In addition, Myong [7] made an in-depth study of the MHD Riemann problem, and Tóth and Odstrcil [8] compared various schemes for MHD.

One of the issues that remains to be resolved for this class of schemes for ideal MHD is the method by which the $\nabla \cdot \mathbf{B}$ constraint is enforced [9]. One approach is that of a Hodge projection, in which the magnetic field is split into the sum of the gradient of a scalar and the curl of a vector, resulting in a Poisson equation for the scalar, such that the constraint is enforced (see, for example, [10]). Another approach is to employ a staggered grid, such as that used in the constrained transport technique [11]. Hybrid methods that used constrained transport combined with a Godunov scheme have also been recently developed [12]. In the work presented here, an alternative method is put forward. The ideal MHD equations are solved in their symmetrizable form. This form, first derived by Godunov [13], allows the derivation of an approximate Riemann solver with eight waves [14]. The resulting Riemann solver, described in detail in this paper, maintains zero divergence of the magnetic field (a necessary initial condition) to truncation-error levels, even for long integration times.

In the following sections, the governing equations are given in the form used here, and an eight-wave Roe-type approximate Riemann solver is derived from them. A solution-adaptive scheme with the approximate Riemann solver as its basic building block is described and validated for several cases. In addition, a method for subtracting out an embedded steady magnetic field is described and used in solving for the interaction of the solar wind with a magnetized planet.

2. GOVERNING EQUATIONS

The governing equations for ideal MHD in three dimensions are statements of

- conservation of mass (1 equation)
- conservation of momentum (3 equations)
- Faraday's law (3 equations), and
- conservation of energy (1 equation)

for an ideal, inviscid, perfectly conducting fluid moving at non-relativistic speeds. These eight equations are expressed in terms of eight dependent variables:

- density (ρ),
- x-, y-, and z-components of momentum (ρu, ρv, and ρw),
- x-, y-, and z-components of magnetic field (B_x, B_y, and B_z),
- and total plasma energy (E),

where

$$E = \rho e + \rho \frac{\mathbf{u} \cdot \mathbf{u}}{2} + \frac{\mathbf{B} \cdot \mathbf{B}}{2\mu_0}. \tag{1}$$

In addition, the ideal-gas equation of state

$$e = \frac{p}{(\gamma - 1)\rho} \tag{2}$$

is used to relate pressure and energy, and Ampère's law is used to relate magnetic field and current density.

The ideal MHD equations, in the form they are used for this work, are given below. Vinokur [15] has carried out a careful derivation, including effects of non-idealities, that goes beyond what is given here.

2.1. Conservation of Mass

The conservation of mass for a plasma is the same as that for a fluid, i.e.,

$$\frac{\partial \rho}{\partial t} + \nabla \cdot (\rho \mathbf{u}) = 0. \tag{3}$$

2.2. Faraday's Law

In a moving medium, the total time rate of change of the magnetic flux across a given surface S bounded by curve ∂S is [16]

$$\frac{d}{dt} \int_S \mathbf{B} \cdot \mathbf{dS} = \int_S \frac{\partial \mathbf{B}}{\partial t} \cdot \mathbf{dS} + \oint_{\partial S} \mathbf{B} \times \mathbf{u} \cdot dl + \int_S \nabla \cdot \mathbf{B}\mathbf{u} \cdot \mathbf{dS}, \tag{4}$$

where the third term on the right-hand side arises from the passage of the surface S through an inhomogeneous vector field in which flux lines are generated. Using Stokes' theorem, and the fact that E' is zero in the co-moving frame, Faraday's law,

$$-\frac{d}{dt} \int_S \mathbf{B} \cdot \mathbf{dS} = \oint_{\partial S} \mathbf{E}' \cdot dl \tag{5}$$

becomes

$$\frac{\partial \mathbf{B}}{\partial t} + \nabla \cdot (\mathbf{u}\mathbf{B} - \mathbf{B}\mathbf{u}) = -\mathbf{u}\nabla \cdot \mathbf{B}. \tag{6}$$

The term $\mathbf{u}\nabla \cdot \mathbf{B}$, which is typically dropped in the derivation due to the absence of magnetic monopoles, is kept here for reasons to be discussed in Subsection 2.8.

2.3. Conservation of Momentum

Conservation of momentum in differential form is

$$\frac{\partial (\rho \mathbf{u})}{\partial t} + \nabla \cdot (\rho \mathbf{u}\mathbf{u} + p\mathbf{I}) = \mathbf{j} \times \mathbf{B}. \tag{7}$$

Under the assumptions of ideal MHD, Ampère's law is

$$\mathbf{j} = \frac{1}{\mu_0} \nabla \times \mathbf{B}, \tag{8}$$

where μ_0 is the permeability of vacuum. Thus, conservation of momentum for ideal MHD can be written

$$\frac{\partial(\rho\mathbf{u})}{\partial t} + \nabla \cdot (\rho\mathbf{u}\mathbf{u} + p\mathbf{I}) = \frac{1}{\mu_0}(\nabla \times \mathbf{B}) \times \mathbf{B}. \tag{9}$$

Rewriting Eq. (9), using a vector identity for $(\nabla \times \mathbf{B}) \times \mathbf{B}$, gives

$$\frac{\partial(\rho\mathbf{u})}{\partial t} + \nabla \cdot \left(\rho\mathbf{u}\mathbf{u} + \left(p + \frac{\mathbf{B} \cdot \mathbf{B}}{2\mu_0} \right) \mathbf{I} - \frac{\mathbf{B}\mathbf{B}}{\mu_0} \right) = -\frac{1}{\mu_0}\mathbf{B}\nabla \cdot \mathbf{B}. \tag{10}$$

As with Faraday's law, a term proportional to $\nabla \cdot \mathbf{B}$ is retained for reasons discussed in Subsection 2.8.

2.4. Conservation of Energy

Conservation of hydrodynamic energy density,

$$E_{hd} = \rho e + \rho\frac{\mathbf{u} \cdot \mathbf{u}}{2} \tag{11}$$

$$= \frac{p}{\gamma - 1} + \rho\frac{\mathbf{u} \cdot \mathbf{u}}{2} \tag{12}$$

for a fixed control volume of conducting fluid is given by

$$\frac{\partial E_{hd}}{\partial t} + \nabla \cdot (\mathbf{u}(E_{hd} + p)) = \mathbf{j} \cdot \mathbf{E}. \tag{13}$$

Using Ampère's law and the identity

$$\mathbf{E} \times \mathbf{B} = (\mathbf{B} \cdot \mathbf{B})\mathbf{u} - (\mathbf{u} \cdot \mathbf{B})\mathbf{B},$$

the $\mathbf{j} \cdot \mathbf{E}$ term can be expressed in terms of $\mathbf{u}$ and $\mathbf{B}$ as

$$\mathbf{j} \cdot \mathbf{E} = \frac{1}{\mu_0} \left[\mathbf{B} \cdot \frac{\partial \mathbf{B}}{\partial t} - (\mathbf{u} \cdot \mathbf{B})\nabla \cdot \mathbf{B} - \nabla \cdot ((\mathbf{B} \cdot \mathbf{B})\mathbf{u} - (\mathbf{u} \cdot \mathbf{B})\mathbf{B}) \right].$$

Finally, defining the total energy density of the plasma

$$E = E_{hd} + \frac{\mathbf{B} \cdot \mathbf{B}}{2\mu_0} \tag{14}$$

$$= \frac{p}{\gamma - 1} + \rho\frac{\mathbf{u} \cdot \mathbf{u}}{2} + \frac{\mathbf{B} \cdot \mathbf{B}}{2\mu_0} \tag{15}$$

the energy equation becomes

$$\frac{\partial E}{\partial t} + \nabla \cdot \left[\left(E + p + \frac{\mathbf{B} \cdot \mathbf{B}}{2\mu_0} \right) \mathbf{u} - \frac{1}{\mu_0}(\mathbf{u} \cdot \mathbf{B})\mathbf{B} \right] = -\frac{1}{\mu_0}(\mathbf{u} \cdot \mathbf{B})\nabla \cdot \mathbf{B}. \tag{16}$$

2.5. *Non-dimesionalization*

It is usual to non-dimensionalize the ideal MHD equations, using, for example, L (a reference length), a_∞ (the free-stream ion-acoustic speed), and ρ_∞ (the free-stream density). In addition, the current and magnetic field are scaled with $\sqrt{\mu_0}$, which results in the removal of μ_0 from the equations. This non-dimensional scaled form of the equations is used from this point on in this paper.

2.6. *Quasilinear Form of Equations*

For the eigensystem analysis necessary to develop the Riemann solver, it is convenient to write the governing equations as a quasilinear system in the primitive variables,

$$\mathbf{W} = (\rho, u, v, w, B_x, B_y, B_z, p)^T. \tag{17}$$

The primitive variables can be related to the vector of conserved variables

$$\mathbf{U} = (\rho, \rho u, \rho v, \rho w, B_x, B_y, B_z, E)^T \tag{18}$$

by the Jacobian matrices

$$\frac{\partial \mathbf{U}}{\partial \mathbf{W}} = \begin{bmatrix} 1 & 0 & 0 & 0 & 0 & 0 & 0 & 0 \\ u & \rho & 0 & 0 & 0 & 0 & 0 & 0 \\ v & 0 & \rho & 0 & 0 & 0 & 0 & 0 \\ w & 0 & 0 & \rho & 0 & 0 & 0 & 0 \\ 0 & 0 & 0 & 0 & 1 & 0 & 0 & 0 \\ 0 & 0 & 0 & 0 & 0 & 1 & 0 & 0 \\ 0 & 0 & 0 & 0 & 0 & 0 & 1 & 0 \\ \frac{\mathbf{u} \cdot \mathbf{u}}{2} & \rho u & \rho v & \rho w & B_x & B_y & B_z & \frac{1}{\gamma - 1} \end{bmatrix} \tag{19}$$

$$\frac{\partial \mathbf{W}}{\partial \mathbf{U}} = \begin{bmatrix} 1 & 0 & 0 & 0 & 0 & 0 & 0 & 0 \\ -\frac{u}{\rho} & \frac{1}{\rho} & 0 & 0 & 0 & 0 & 0 & 0 \\ -\frac{v}{\rho} & 0 & \frac{1}{\rho} & 0 & 0 & 0 & 0 & 0 \\ -\frac{w}{\rho} & 0 & 0 & \frac{1}{\rho} & 0 & 0 & 0 & 0 \\ 0 & 0 & 0 & 0 & 1 & 0 & 0 & 0 \\ 0 & 0 & 0 & 0 & 0 & 1 & 0 & 0 \\ 0 & 0 & 0 & 0 & 0 & 0 & 1 & 0 \\ \frac{(\gamma-1)}{2} \mathbf{u} \cdot \mathbf{u} & ku & kv & kw & kB_x & kB_y & kB_z & (\gamma - 1) \end{bmatrix}, \tag{20}$$

where $k = (1 - \gamma)$.

Collecting Eqs. (3), (6), (9), and (13), performing the non-dimensionalization, and expressing them in terms of primitive variables gives

$$\frac{\partial \mathbf{W}}{\partial t} + \left(\mathbf{A_x}, \mathbf{A_y}, \mathbf{A_z}\right) \cdot \nabla \mathbf{W} = 0, \tag{21}$$

where

$$\mathbf{A_x} = \begin{bmatrix} u & \rho & 0 & 0 & 0 & 0 & 0 & 0 \\ 0 & u & 0 & 0 & 0 & \frac{B_y}{\rho} & \frac{B_z}{\rho} & \frac{1}{\rho} \\ 0 & 0 & u & 0 & 0 & -\frac{B_x}{\rho} & 0 & 0 \\ 0 & 0 & 0 & u & 0 & 0 & -\frac{B_x}{\rho} & 0 \\ 0 & 0 & 0 & 0 & u & 0 & 0 & 0 \\ 0 & B_y & -B_x & 0 & 0 & u & 0 & 0 \\ 0 & B_z & 0 & -B_x & 0 & 0 & u & 0 \\ 0 & \gamma p & 0 & 0 & 0 & 0 & 0 & u \end{bmatrix}$$

$$\mathbf{A_y} = \begin{bmatrix} v & 0 & \rho & 0 & 0 & 0 & 0 & 0 \\ 0 & v & 0 & 0 & -\frac{B_y}{\rho} & 0 & 0 & 0 \\ 0 & 0 & v & 0 & \frac{B_x}{\rho} & 0 & \frac{B_z}{\rho} & \frac{1}{\rho} \\ 0 & 0 & 0 & v & 0 & 0 & -\frac{B_y}{\rho} & 0 \\ 0 & -B_y & B_x & 0 & v & 0 & 0 & 0 \\ 0 & 0 & 0 & 0 & 0 & v & 0 & 0 \\ 0 & 0 & B_z & -B_y & 0 & 0 & v & 0 \\ 0 & 0 & \gamma p & 0 & 0 & 0 & 0 & v \end{bmatrix} \qquad (22)$$

$$\mathbf{A_z} = \begin{bmatrix} w & 0 & 0 & \rho & 0 & 0 & 0 & 0 \\ 0 & w & 0 & 0 & -\frac{B_z}{\rho} & 0 & 0 & 0 \\ 0 & 0 & w & 0 & 0 & -\frac{B_z}{\rho} & 0 & 0 \\ 0 & 0 & 0 & w & \frac{B_x}{\rho} & \frac{B_y}{\rho} & 0 & \frac{1}{\rho} \\ 0 & -B_z & 0 & B_x & w & 0 & 0 & 0 \\ 0 & 0 & -B_z & B_y & 0 & w & 0 & 0 \\ 0 & 0 & 0 & 0 & 0 & 0 & w & 0 \\ 0 & 0 & 0 & \gamma p & 0 & 0 & 0 & w \end{bmatrix} .$$

2.7. Divergence Form of Equations

Collecting Eqs. (3), (6), (10), and (16), and applying the non-dimensionalization, the normalized divergence form

$$\frac{\partial \mathbf{U}}{\partial t} + (\nabla \cdot \mathbf{F})^T = \mathbf{S}, \qquad (23)$$

may be written, where $\mathbf{U}$ is the vector of conserved quantities defined by Eq. (18), $\mathbf{F}$ is a flux tensor,

$$\mathbf{F} = \begin{pmatrix} \rho\mathbf{u} \\ \rho\mathbf{uu} + \left(p + \frac{\mathbf{B}\cdot\mathbf{B}}{2}\right)\mathbf{I} - \mathbf{BB} \\ \mathbf{uB} - \mathbf{Bu} \\ \mathbf{u}\left(E + p + \frac{\mathbf{B}\cdot\mathbf{B}}{2}\right) - (\mathbf{u}\cdot\mathbf{B})\mathbf{B} \end{pmatrix}^T, \qquad (24)$$

and **S** is a "source" vector, containing the terms that cannot be expressed in divergence form:

$$
\mathbf{S} = -\nabla \cdot \mathbf{B} \begin{pmatrix} 0 \\ \mathbf{B} \\ \mathbf{u} \\ \mathbf{u} \cdot \mathbf{B} \end{pmatrix}.
\tag{25}
$$

2.8. *A Note on the* $\nabla \cdot \mathbf{B}$ *Source Term in the Divergence Form*

The terms proportional to $\nabla \cdot \mathbf{B}$ in Eq. (23) arise solely from rewriting the magnetic-field terms in the governing equations in divergence form. Eqution (23) (*with* the source term) is exactly equivalent to Eq. (21). Although for physical fields there are no magnetic monopoles, and the source term is therefore zero, dropping the source term from the analysis changes the character of the equations. This has been pointed out previously by Godunov [13]. He found that the ideal MHD equations written in pure divergence form (i.e., Eq. (23) *without* the source term) are not symmetrizable. He further found that the system could be rendered symmetrizable only by adding a factor of the constraint $\nabla \cdot \mathbf{B} = 0$ to each of the equations, and that the resulting symmetrizable form was that of Eq. (23) *with* the source term.

Symmetrizable systems of conservation laws have been studied by Godunov [17] and Harten [18], among others. One property of the symmetrizable form of a system of conservation laws is that an added conservation law

$$
\frac{\partial(\rho s)}{\partial t} + \frac{\partial(\rho u s)}{\partial x} + \frac{\partial(\rho v s)}{\partial y} + \frac{\partial(\rho w s)}{\partial z} = 0
$$

for the entropy s can be derived by multiplying each equation in the system by a factor and adding the resulting equations. For the ideal MHD equations, as for the gasdynamic equations, the entropy is $s = \log(p/\rho^\gamma)$. Another property is that the system is Gallilean invariant; all waves in the system propagate at speeds $u \pm c$ (for MHD, the possible values of c are the Alfvén, magnetofast, and magentoslow speeds, described below). Neither of these properties holds for the MHD system if the source term is ignored.

Eq. (21), or Eq. (23) *with* the source term, yields the following evolution equation for $\nabla \cdot \mathbf{B}$:

$$
\frac{\partial}{\partial t}(\nabla \cdot \mathbf{B}) + \nabla \cdot (\mathbf{u}\nabla \cdot \mathbf{B}) = 0.
\tag{26}
$$

This is a statement that the quantity $\nabla \cdot \mathbf{B}/\rho$ satisfies the equation for a passively convected scalar ϕ, i.e.,

$$
\frac{\partial}{\partial t}(\rho\phi) + \nabla \cdot (\rho\mathbf{u}\phi) = 0.
\tag{27}
$$

Thus, for a solution of this system, the quantity $\nabla \cdot \mathbf{B}/\rho$ is constant along particle paths and therefore, since the initial and boundary conditions satisfy $\nabla \cdot \mathbf{B} = 0$, the same will be true for all later times throughout the flow. The only ambiguity arises in regions which are cut off from the boundaries, i.e., isolated regions of recirculating flow. These can occur in three-dimensional flow fields and do in some of the cases that have been run. In practice,

these regions do not lead to numerical difficulties. This may be due to the fact that, in a numerical calculation, these regions are not truly isolated from the outer flow, due to numerical dissipation. Thus, although not connected to the outer flow via a streamline, the magnetic field inside the recirculating region must be compatible with that of the outer flow. This remains to be proven, however.

The downside of the solving the equations in the form given in Eq. (23) is, of course, that they are not strictly conservative. Terms of order $\nabla \cdot \mathbf{B}$ are added to what would otherwise be a divergence form. The danger of this is that shock jump conditions may not be correctly met, unless the added terms are small, and/or they alternate in sign in such a way that the errors are local, and in a global sense cancel in some way with neighboring terms. This downside, however, has to be weighed against the alternative; a system (i.e., the one without the source term) that, while conservative, is not Gallilean invariant, has a zero eigenvalue in the Jacobian matrix, and is not symmetrizable.

The approach taken in this paper is therefore to solve the equations in their symmetrizable form, i.e., the form of Eq. (23). As shown previously [14], this form of the equations allows the derivation of an eight-wave approximate Riemann solver that can be used to construct an upwind solution scheme for multi-dimensional flows. The elements of the solution scheme are described in the following section.

3. ELEMENTS OF SOLUTION SCHEME

3.1. *Overview of Scheme*

The scheme described here is an explicit, solution-adaptive, high-resolution, upwind finite-volume scheme. In a finite-volume approach, the governing equations in the form of Eq. (23) are integrated over a cell in the grid, giving

$$\int_{cell\,i} \frac{\partial \mathbf{U}}{\partial t}\, dV + \int_{cell\,i} \nabla \cdot \mathbf{F}\, dV = \int_{cell\,i} \mathbf{S}\, dV \tag{28}$$

$$\frac{d\mathbf{U}_i}{dt} V_i + \oint_{\partial(cell\,i)} \mathbf{F} \cdot \hat{\mathbf{n}}\, dS = \mathbf{S}_i V_i, \tag{29}$$

where $\mathbf{U}_i$ and $\mathbf{S}_i$ are the cell-averaged conserved variables and source terms, respectively, V_i is the cell volume, and $\hat{\mathbf{n}}$ is a unit normal vector, pointing outward from the boundary of the cell. In order to evaluate the integral, a quadrature scheme must be chosen; a simple midpoint rule is used here, giving

$$\frac{d\mathbf{U}_i}{dt} V_i + \sum_{faces} \mathbf{F} \cdot \hat{\mathbf{n}}\, dS = \mathbf{S}_i V_i, \tag{30}$$

where the $\mathbf{F} \cdot \hat{\mathbf{n}}$ terms are evaluated at the midpoints of the faces of the cell. The source term $\mathbf{S}_i$ is proportional to the volume average of $\nabla \cdot \mathbf{B}$ for a cell. That average is computed by

$$\nabla \cdot \mathbf{B}_{cell\,i} = \frac{1}{V_i} \sum_{faces} \mathbf{B} \cdot \hat{\mathbf{n}}\, dS;$$

the equation to be integrated in time is therefore

$$\frac{d\mathbf{U}_i}{dt} V_i + \sum_{faces} \mathbf{F} \cdot \hat{\mathbf{n}} \, dS = - \begin{pmatrix} 0 \\ \mathbf{B} \\ \mathbf{u} \\ \mathbf{u} \cdot \mathbf{B} \end{pmatrix}_i \sum_{faces} \mathbf{B} \cdot \hat{\mathbf{n}} \, dS. \tag{31}$$

The evaluation of $\mathbf{F} \cdot \hat{\mathbf{n}}$ at the interface is done by a Roe scheme for MHD, as described in Subsection 3.5. Other approximate Riemann solvers have been used in the code described here, including an MHD version of the HLLE scheme [6]. These solvers are all based on the eigensystem of the symmetric equations, described in Subsection 3.5. The time-integration scheme for Eq. (30), the solution-adaptive technique, and the limited reconstruction technique that makes the scheme second order in space are also described in the following sections.

3.2. Grid and Data Structure

The grid used in this work is an adaptive Cartesian one, with an underlying tree data structure. The basic underlying unit is a block of structured grid of arbitrary size. In the limit, the patch could be $1 \times 1 \times 1$, i.e., a single cell; more typically, blocks of anywhere from $4 \times 4 \times 4$ cells to $10 \times 10 \times 10$ cells are used. Each grid block corresponds to a node of the tree: the root of the tree is a single coarse block of structured grid covering the entire solution domain. In regions flagged for refinement, a block is divided into eight octants; in each octant, Δx, Δy, and Δz are each halved from their value on the "parent" block. Two neighboring blocks, one of which has been refined and one of which has not, are shown in Fig. 1. Any of these blocks can in turn be refined, and so on, building up a tree of successively finer blocks. The data structure is described more fully elsewhere [19]. The approach closely follows that first developed for two-dimensional gas dynamics calculations by Berger *et al.* [20–22].

This block-based tree data structure is advantageous for two primary reasons. One is the ease with which the grid can be adapted. If, at some point in the calculation, a particular region of the flow is deemed to be sufficiently interesting, better resolution of that region can be attained by refining a block, and inserting the eight finer blocks that result from this refinement into the data structure. Removing refinement in a region is equally easy. Decisions as to where to refine and coarsen are made based on comparison of local flow quantities to threshold values. Refinement criteria used in this work are local values of

$$\epsilon_c = |\nabla \cdot \mathbf{u}| / \sqrt{V}$$
$$\epsilon_r = |\nabla \times \mathbf{u}| / \sqrt{V} \tag{32}$$
$$\epsilon_t = |\nabla \times \mathbf{B}| / \sqrt{V}.$$

These represent local measures of compressibility, rotationality, and current density. V is the cell volume; a scaling of this type is necessary to allow the scheme to resolve smooth regions of the flow as well as discontinuous ones [23].

Another advantage of this approach is ease of parallelization: blocks of the grid can easily be farmed out to separate processors, with communication limited to the boundary between
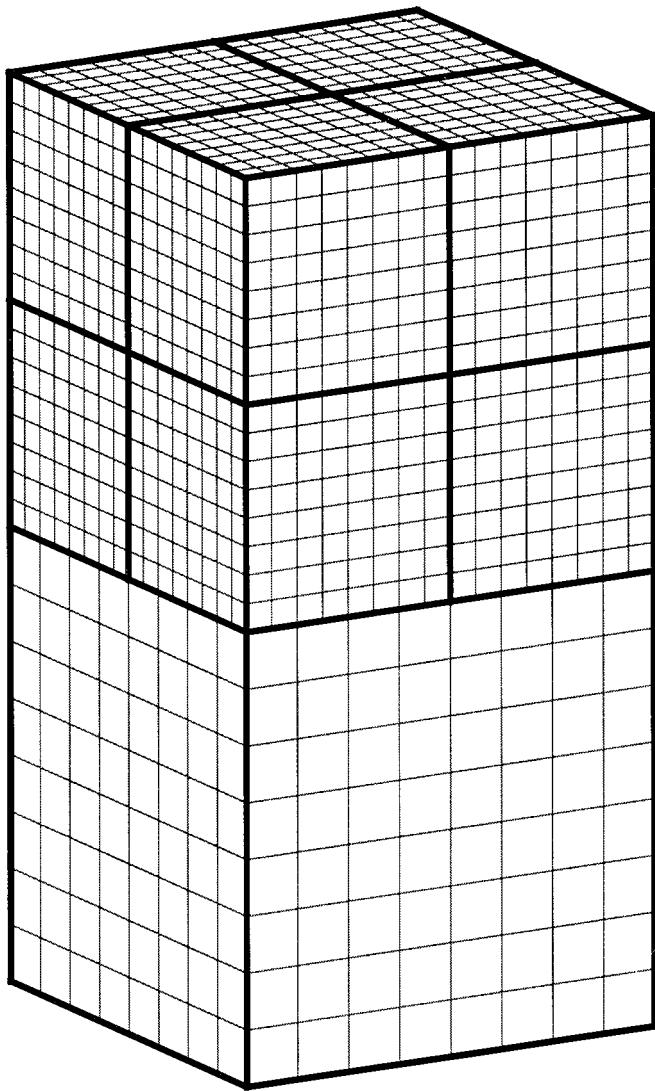
FIG. 1. Example of neighboring refined and unrefined blocks.

a block and its parent [24, 19]. The number of cells in the refinement blocks can be chosen so as to facilitate load balancing; in particular, an octant of a block is typically refined, so that each block of cells in the grid has the same number of cells [19].

3.3. *Limited Linear Reconstruction*

In order for the scheme to be more than first-order accurate, a local reconstruction must be done; in order for the scheme to yield oscillation-free results, the reconstruction must be limited. The limited linear reconstruction described here is due to Barth [25]. A least-squares gradient is calculated, using the cell-centered values in neighboring cells, by locally solving the following non-square system for the gradient of the kth component of the primitive

variable vector W by a least-squares approach

$$\mathcal{L} \nabla W^{(k)} = f \tag{33}$$

$$\mathcal{L} = \begin{pmatrix} \Delta x_1 & \Delta y_1 & \Delta z_1 \\ \vdots & \vdots & \vdots \\ \Delta x_N & \Delta y_N & \Delta z_N \end{pmatrix}, \qquad f = \begin{pmatrix} \Delta W_1^{(k)} \\ \vdots \\ \Delta W_N^{(k)} \end{pmatrix}, \tag{34}$$

where

$$\Delta x_i = x_i - x_0$$
$$\Delta y_i = y_i - y_0$$
$$\Delta z_i = z_i - z_0$$
$$\Delta W_i^{(k)} = \bar{W}_i^{(k)} - \bar{W}_0^{(k)}$$

and the points are numbered so that 0 is the cell in which the gradient is being calculated, and i is one of N neighboring cells used in the reconstruction.

The gradients calculated in this manner must be limited in order to avoid overshoots. A typical choice is a limiter due to Barth [25]. The reconstructed values are limited by a quantity $\phi^{(k)}$ in the following way

$$W^{(k)}(\mathbf{x}) = \bar{W}^{(k)} + \phi^{(k)}(\mathbf{x} - \bar{\mathbf{x}}) \cdot \nabla W^{(k)}, \tag{35}$$

where $\phi^{(k)}$ is given by

$$\phi^{(k)} = \min\left(1, \frac{\left|\bar{W}^{(k)} - \max_{neighbors}\left(\bar{W}^{(k)}\right)\right|}{\left|\bar{W}^{(k)} - \max_{cell}\left(W^{(k)}\right)\right|}, \frac{\left|\bar{W}^{(k)} - \min_{neighbors}\left(\bar{W}^{(k)}\right)\right|}{\left|\bar{W}^{(k)} - \min_{cell}\left(W^{(k)}\right)\right|}\right). \tag{36}$$

In the above, $\bar{W}^{(k)}$ is the value of the kth component of $\mathbf{W}$ at a cell center $\bar{\mathbf{x}}$, the subscript *neighbors* denotes the neighboring cells used in the gradient reconstruction, and the subscript *cell* denotes the unlimited ($\phi = 1$) reconstruction to the centroids of the faces of the cell.

At the interfaces of blocks that are at different refinement levels, states are constructed in two layers of "ghost cells" so that the interface is transparent to the reconstruction described above. Since refinement level differences of greater than one are not allowed, there are only two types of ghost cells: those created for a coarse block from values on a neighboring finer block, and those created for a fine block from values on a neighboring coarser block. A simple trilinear interpolation is used to construct the values in the ghost cells.

3.4. *Multi-stage Time Stepping*

The time-stepping scheme used is one of the optimally smoothing multi-stage schemes developed by Van Leer *et al.* [26]. The general m-stage scheme for integrating Eq. (30) from time-level n to time-level $n + 1$ is

$$\mathbf{U}^{(0)} = \mathbf{U}^n \tag{37}$$

$$\mathbf{U}^{(k)} = \mathbf{U}^{(0)} + \alpha_k \Delta t \mathbf{R}\left(\mathbf{U}^{(k-1)}\right), \qquad k = 1 \cdots m \tag{38}$$

$$\mathbf{U}^{(n+1)} = \mathbf{U}^{(m)}, \tag{39}$$

where

$$\mathbf{R} = \mathbf{S}_i - \frac{1}{V_i} \sum_{faces} \mathbf{F} \cdot \hat{\mathbf{n}} \, dS.$$

The multi-stage coefficients α_k and the associated time-step constraint are those that give optimal smoothing of high-frequency error modes in the solution, thereby accelerating convergence to a steady state [27]. Typically, the two-stage optimal second-order scheme is used. For this scheme, $\alpha_1 = 0.4242$, $\alpha_2 = 1.0$, and the corresponding CFL number used to choose Δt is 0.4693. This approach is, of course, only used when steady-state solutions are desired; for unsteady problems, the second-order in time two-step scheme ($\alpha_1 = 0.5$, $\alpha_2 = 1.0$) is used.

3.5. Approximate Riemann Solver

An approximate Riemann solver is used to compute the interface fluxes needed for the finite-volume scheme of Eq. 30. A Roe scheme is used here; it is based on the eigensystem of the matrix

$$\mathbf{A_n} = (\mathbf{A_x}, \mathbf{A_y}, \mathbf{A_z}) \cdot \hat{\mathbf{n}}, \tag{40}$$

where $\mathbf{A_x}$, $\mathbf{A_y}$, and $\mathbf{A_z}$ are the matrices in the quasilinear form of the equations (Eq. (21)) and $\hat{\mathbf{n}}$ is the normal to the face for which the flux is being computed. For simplicity, the derivation is done here for $\hat{\mathbf{n}} = \hat{\mathbf{x}}$; results for an arbitrarily aligned face can be obtained by use of a simple rotation matrix.

3.5.1. Eigensystem of the governing equations. For the matrix $\mathbf{A} \cdot \hat{\mathbf{x}}$, there are eight waves, with their corresponding eigenvalues λ, left eigenvectors l, and right eigenvectors r. The eigenvalues are:

- $\lambda_e = u$, corresponding to an entropy wave;
- $\lambda_d = u$, corresponding to a magnetic-flux wave;
- $\lambda_a = u \pm B_x/\sqrt{\rho}$, corresponding to a pair of Alfvén waves; and
- $\lambda_{f,s} = u \pm c_{f,s}$, corresponding to two pairs of magneto-acoustic waves.

The magneto-acoustic speeds are given by

$$c_{f,s} = \sqrt{\frac{1}{2} \left(\frac{\gamma p + \mathbf{B} \cdot \mathbf{B}}{\rho} \pm \sqrt{\left(\frac{\gamma p + \mathbf{B} \cdot \mathbf{B}}{\rho} \right)^2 - 4 \frac{\gamma p B_x^2}{\rho^2}} \right)}.$$

The eigenvectors corresponding to these waves are unique only up to a scaling factor. A suitable choice of scaling is given by Roe and Balsara [3]; that choice was used in the current work. (Recently, Barth [28] introduced a scaling that is slightly better conditioned.) The scaled version of the eigenvectors comes from defining

$$\alpha_f^2 = \frac{a^2 - c_s^2}{c_f^2 - c_s^2}, \qquad \alpha_s^2 = \frac{c_f^2 - a^2}{c_f^2 - c_s^2} \tag{41}$$

and

$$\beta_y = \frac{B_y}{\sqrt{B_y^2 + B_z^2}}, \qquad \beta_z = \frac{B_z}{\sqrt{B_y^2 + B_z^2}}. \tag{42}$$

The scaled eigenvectors are:
Entropy,

$$\lambda_e = u$$
$$l_e = \left(1, 0, 0, 0, 0, 0, 0, -\frac{1}{a^2}\right) \tag{43}$$
$$r_e = (1, 0, 0, 0, 0, 0, 0, 0)^T.$$

Magnetic Flux,

$$\lambda_d = u$$
$$l_d = (0, 0, 0, 0, 1, 0, 0, 0) \tag{44}$$
$$r_d = (0, 0, 0, 0, 1, 0, 0, 0)^T.$$

Alfvén,

$$\lambda_a = u \pm \frac{B_x}{\rho}$$
$$l_a = \left(0, 0, -\frac{\beta_z}{\sqrt{2}}, \frac{\beta_y}{\sqrt{2}}, 0, \pm\frac{\beta_z}{\sqrt{2\rho}}, \mp\frac{\beta_y}{\sqrt{2\rho}}, 0\right) \tag{45}$$
$$r_a = \left(0, 0, -\frac{\beta_z}{\sqrt{2}}, \frac{\beta_y}{\sqrt{2}}, 0, \pm\sqrt{\frac{\rho}{2}}\beta_z, \mp\sqrt{\frac{\rho}{2}}\beta_y, 0\right)^T.$$

Fast,

$$\lambda_f = u \pm c_f$$
$$l_f = \left(0, \pm\frac{\alpha_f c_f}{2a^2}, \mp\frac{\alpha_s}{2a^2}c_s\beta_y\,\mathrm{sgn}B_x, \mp\frac{\alpha_s}{2a^2}c_s\beta_z\,\mathrm{sgn}B_x, 0,\right.$$
$$\left.\frac{\alpha_s}{2\sqrt{\rho}a}\beta_y, \frac{\alpha_s}{2\sqrt{\rho}a}\beta_z, \frac{\alpha_f}{2\rho a^2}\right) \tag{46}$$
$$r_f = (\rho\alpha_f, \pm\alpha_f c_f, \mp\alpha_s c_s\beta_y\,\mathrm{sgn}B_x, \mp\alpha_s c_s\beta_y\,\mathrm{sgn}B_x, 0,$$
$$\alpha_s\sqrt{\rho}a\beta_y, \alpha_s\sqrt{\rho}a\beta_z, \alpha_f\gamma p)^T.$$

Slow,

$$\lambda_s = u \pm c_s$$
$$l_s = \left(0, \pm\frac{\alpha_s c_s}{2a^2}, \pm\frac{\alpha_f}{2a^2}c_f\beta_y\,\mathrm{sgn}B_x, \pm\frac{\alpha_f}{2a^2}c_f\beta_z\,\mathrm{sgn}B_x, 0,\right.$$
$$\left.-\frac{\alpha_f}{2\sqrt{\rho}a}\beta_y, -\frac{\alpha_f}{2\sqrt{\rho}a}\beta_z, \frac{\alpha_s}{2\rho a^2}\right) \tag{47}$$
$$r_s = (\rho\alpha_s, \pm\alpha_s c_s, \pm\alpha_f c_f\beta_y\,\mathrm{sgn}B_x, \pm\alpha_f c_f\beta_z\,\mathrm{sgn}B_x, 0,$$
$$-\alpha_f\sqrt{\rho}a\beta_y, -\alpha_f\sqrt{\rho}a\beta_z, \alpha_s\gamma p)^T.$$

The eigenvectors given above are orthonormal, and, since α_f, α_s, β_y, and β_z all lie between zero and one, the eigenvectors are all well-formed, once these four parameters are defined. The only difficulties in defining these occur when $B_y^2 + B_z^2 = 0$, in which case β_y and β_z are ill-defined, and when $B_y^2 + B_z^2 = 0$ *and* $B_x^2 = \rho a^2$, in which case α_s and α_f are ill-defined. The first case is fairly trivial; β_y and β_z represent direction cosines for the tangential component of the B-field, and in the case of a zero component, it is only important to choose so that $\beta_y^2 + \beta_z^2 = 1$. The choice used here is the same as that proposed by Brio and Wu [1],

$$\beta_y = \frac{1}{\sqrt{2}}, \qquad \beta_z = \frac{1}{\sqrt{2}}. \tag{48}$$

An approach for the case in which α_s and α_f are ill-defined is outlined by Roe and Balasara [3]. No special treatment of this type was needed for the cases shown in this paper. Indeed, it is shown in [3] that although the linearized Riemann problem has multiple solutions in this case, they all give the same value for the interface flux.

3.5.2. Construction of the flux function.   The flux function used in this work is defined in the manner of Roe [29] as

$$\mathbf{F} \cdot \hat{\mathbf{n}}(\mathbf{U}_L, \mathbf{U}_R) = \frac{1}{2}(\mathbf{F} \cdot \hat{\mathbf{n}}(\mathbf{U}_L) + \mathbf{F} \cdot \hat{\mathbf{n}}(\mathbf{U}_R)) - \sum_{k=1}^{8} \mathbf{L}_k(\mathbf{U}_R - \mathbf{U}_L)|\lambda_k|\mathbf{R}_k, \tag{49}$$

where k is an index for the loop over the entropy, divergence, Alvén, magneto-acoustic waves. The conservative eigenvectors are

$$\mathbf{L}_k = l_k \frac{\partial \mathbf{W}}{\partial \mathbf{U}} \tag{50}$$

$$\mathbf{R}_k = \frac{\partial \mathbf{U}}{\partial \mathbf{W}} r_k. \tag{51}$$

In Eq. (49), the terms denoted with subscripts L and R are evaluated from the face-midpoint states just to the left and right of the interface, as determined by the limited linear reconstruction procedure described above. The eigenvalues and eigenvectors are evaluated at an "interface" state that is some combination of the L and R states. For gas dynamics, there is a unique interface state (the "Roe-average state") that Roe has shown exhibits certain desired properties [29]. For MHD, while some interesting work has been done on finding an analogous state for MHD (see, for example, [30]), a unique, efficiently computable Roe average is still elusive. In this paper, a simple arithmetic averaging of the primitive variables is done to compute the interface state. Vector variables (velocity, magnetic field) are averaged component by component.

If a so-called "entropy fix" is not applied to Roe's scheme, expansion shocks can be permitted [31]. The entropy fix is applied to the magnetosonic waves to bound those eigenvalues away from zero when the flow is expanding. This is done by replacing $|\lambda_k|$ in Eq. (49) with $|\lambda_k^*|$ (for the values of k corresponding to the magnetoacoustic waves only) where $|\lambda_k^*|$ is given by

$$|\lambda_k^*| = \begin{cases} |\lambda_k|, & |\lambda_k| \geq \frac{\delta\lambda_k}{2} \\ \frac{\lambda_k^2}{\delta\lambda_k} + \frac{\delta\lambda_k}{4}, & |\lambda_k| < \frac{\delta\lambda_k}{2}, \end{cases} \tag{52}$$

where

$$\delta\lambda_k = \max(4(\lambda_{kR} - \lambda_{kL}), 0).$$

4. SOLVING FOR FLOWS WITH EMBEDDED STEADY FIELDS

For problems in which a strong "intrinsic" magnetic field is present, accuracy can be gained by solving for the deviation of the magnetic field from this intrinsic value. For example, in the interaction of the solar wind with a magnetized planet such as earth, the planetary magnetic field, a strong dipole, dominates the magnetic-field pattern near the earth. Solving for the perturbation from the dipole field is inherently more accurate than solving for the full field, then subtracting off the dipole field to calculate the perturbation. This approach, first employed by Tanaka [32], is derived below for the scheme presented in this paper. The derivation here is for a non-rotating body; the technique can be generalized for rotating objects.

Given an "intrinsic" magnetic field, $\mathbf{B}_0$, that satisfies

$$\frac{\partial \mathbf{B}_0}{\partial t} = 0$$
$$\nabla \cdot \mathbf{B}_0 = 0 \qquad\qquad (53)$$
$$\nabla \times \mathbf{B}_0 = 0,$$

the full magnetic field $\mathbf{B}$ may be written as the sum of the intrinsic field and a deviation $\mathbf{B}_1$, i.e.,

$$\mathbf{B} = \mathbf{B}_0 + \mathbf{B}_1. \qquad\qquad (54)$$

Nothing in the following analysis assumes that $\mathbf{B}_1$ is small in relation to $\mathbf{B}_0$.

Primitive and conservative state vectors based on the perturbation field may be defined as

$$\mathbf{W}_1 = (\rho, \mathbf{u}, \mathbf{B}_1, p)^T$$

and

$$\mathbf{U}_1 = (\rho, \rho\mathbf{u}, \mathbf{B}_1, E_1)^T,$$

where

$$E_1 = \frac{p}{\gamma - 1} + \rho\frac{\mathbf{u} \cdot \mathbf{u}}{2} + \frac{\mathbf{B}_1 \cdot \mathbf{B}_1}{2}.$$

Rewriting Eq. (23) in terms of this perturbed state, making no assumptions other than those of Eq. (53), gives

$$\frac{\partial \mathbf{U}_1}{\partial t} + (\nabla \cdot \mathbf{F}_1)^T + (\nabla \cdot \mathbf{G})^T = \mathbf{S}_1, \qquad\qquad (55)$$

where

$$
\mathbf{F}_1 = \begin{pmatrix} \rho\mathbf{u} \\ \rho\mathbf{u}\mathbf{u} + \left(p + \frac{\mathbf{B}_1 \cdot \mathbf{B}_1}{2}\right)\mathbf{I} - \mathbf{B}_1\mathbf{B}_1 \\ \mathbf{u}\mathbf{B}_1 - \mathbf{B}_1\mathbf{u} \\ \mathbf{u}\left(E_1 + p + \frac{\mathbf{B}_1 \cdot \mathbf{B}_1}{2}\right) - (\mathbf{u} \cdot \mathbf{B}_1)\mathbf{B}_1 \end{pmatrix}^T, \tag{56}
$$

$$
\mathbf{S}_1 = -\nabla \cdot \mathbf{B}_1 \begin{pmatrix} 0 \\ \mathbf{B} \\ \mathbf{u} \\ \mathbf{u} \cdot \mathbf{B}_1 \end{pmatrix} \tag{57}
$$

and

$$
\mathbf{G} = \begin{pmatrix} 0 \\ (\mathbf{B}_0 \cdot \mathbf{B}_1)\mathbf{I} - (\mathbf{B}_0\mathbf{B}_1 + \mathbf{B}_1\mathbf{B}_0) \\ \mathbf{u}\mathbf{B}_0 - \mathbf{B}_0\mathbf{u} \\ (\mathbf{B}_0 \cdot \mathbf{B}_1)\mathbf{u} - (\mathbf{u} \cdot \mathbf{B}_1)\mathbf{B}_0 \end{pmatrix}^T. \tag{58}
$$

The quasilinear form of this split system has exactly the same eigenvalues and primitive eigenvectors as in Subsection 3.5. The flux function for the split system therefore differs from that of the original, non-split system only in that the Jacobian matrices relating primitive to conservative variables differ from those of the non-split scheme. Thus, for the split scheme, the flux function is

$$
\mathbf{F}_1 \cdot \hat{\mathbf{n}}(\mathbf{U}_{1_L}, \mathbf{U}_{1_R}) = \frac{1}{2}\left(\mathbf{F}_1 \cdot \hat{\mathbf{n}}(\mathbf{U}_{1_L}) + \mathbf{F}_1 \cdot \hat{\mathbf{n}}(\mathbf{U}_{1_R})\right) - \sum_{k=1}^{8} \mathbf{L}_{1_k}\left(\mathbf{U}_{1_R} - \mathbf{U}_{1_L}\right)|\lambda_k|\mathbf{R}_{1_k}, \tag{59}
$$

where the conservative eigenvectors for the split system are

$$
\mathbf{L}_{1_k} = l_k \frac{\partial \mathbf{W}_1}{\partial \mathbf{U}_1} \tag{60}
$$

$$
\mathbf{R}_{1_k} = \frac{\partial \mathbf{U}_1}{\partial \mathbf{W}_1} r_k \tag{61}
$$

and

$$
\frac{\partial \mathbf{U}_1}{\partial \mathbf{W}_1} = \begin{bmatrix} 1 & 0 & 0 & 0 & 0 & 0 & 0 & 0 \\ u & \rho & 0 & 0 & 0 & 0 & 0 & 0 \\ v & 0 & \rho & 0 & 0 & 0 & 0 & 0 \\ w & 0 & 0 & \rho & 0 & 0 & 0 & 0 \\ 0 & 0 & 0 & 0 & 1 & 0 & 0 & 0 \\ 0 & 0 & 0 & 0 & 0 & 1 & 0 & 0 \\ 0 & 0 & 0 & 0 & 0 & 0 & 1 & 0 \\ \frac{\mathbf{u} \cdot \mathbf{u}}{2} & \rho u & \rho v & \rho w & B_{1x} & B_{1y} & B_{1z} & \frac{1}{\gamma - 1} \end{bmatrix} \tag{62}
$$

$$\frac{\partial \mathbf{W}_1}{\partial \mathbf{U}_1} = \begin{bmatrix} 1 & 0 & 0 & 0 & 0 & 0 & 0 & 0 \\ -\frac{u}{\rho} & \frac{1}{\rho} & 0 & 0 & 0 & 0 & 0 & 0 \\ -\frac{v}{\rho} & 0 & \frac{1}{\rho} & 0 & 0 & 0 & 0 & 0 \\ -\frac{w}{\rho} & 0 & 0 & \frac{1}{\rho} & 0 & 0 & 0 & 0 \\ 0 & 0 & 0 & 0 & 1 & 0 & 0 & 0 \\ 0 & 0 & 0 & 0 & 0 & 1 & 0 & 0 \\ 0 & 0 & 0 & 0 & 0 & 0 & 1 & 0 \\ \frac{(\gamma-1)}{2}\mathbf{u}\cdot\mathbf{u} & ku & kv & kw & kB_{1_x} & kB_{1_y} & kB_{1_z} & (\gamma-1) \end{bmatrix}, \tag{63}$$

where $k = (1 - \gamma)$.

5. VALIDATION OF SCHEME

For the purposes of validation and accuracy assessment, smooth and non-smooth problems with exact solutions were simulated with the method presented in this paper, and the computed solutions for several grids were compared with the exact solutions. The results of the validation runs are presented here.

5.1. Attached Oblique Shocks

Two oblique shock cases were studied: in one, the magnetic field and velocity vectors upstream of the shock are taken to be parallel; in the other, they are perpendicular to each other. For both cases, the acoustic Mach number $M = 5$, the Alfvén number $M_A = 5$, and $\gamma = 5/3$ were taken as the upstream conditions. For both cases, flow past a wedge was computed by the method presented in this paper. The problem is depicted in Fig. 2. Shock polars (i.e., plots of post-shock vertical versus post-shock horizontal velocity components) were constructed by varying the wedge angle and plotting the downstream V_x versus downstream V_y for several wedge angles with the two upstream conditions. Exact shock polars were computed by iteratively solving the appropriate MHD Rankine–Hugoniot relations. Figure 3 is a plot of the exact (solid lines) and computed (symbols) shock polars for the two cases. As is clear from the plot, the agreement is excellent.

In order to assess order of accuracy of the method for non-smooth flows, a single case ($M = 5$, $M_A = 5$, $10°$ wedge, upstream magnetic field, and velocity parallel) was run on a
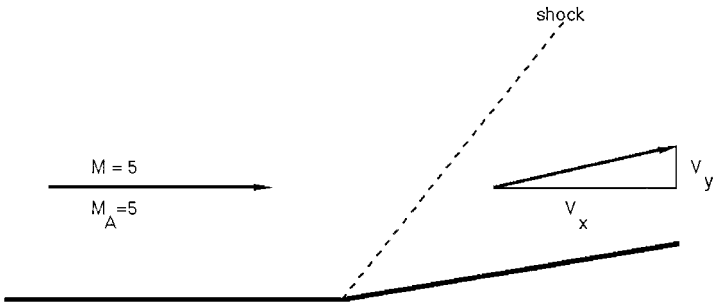

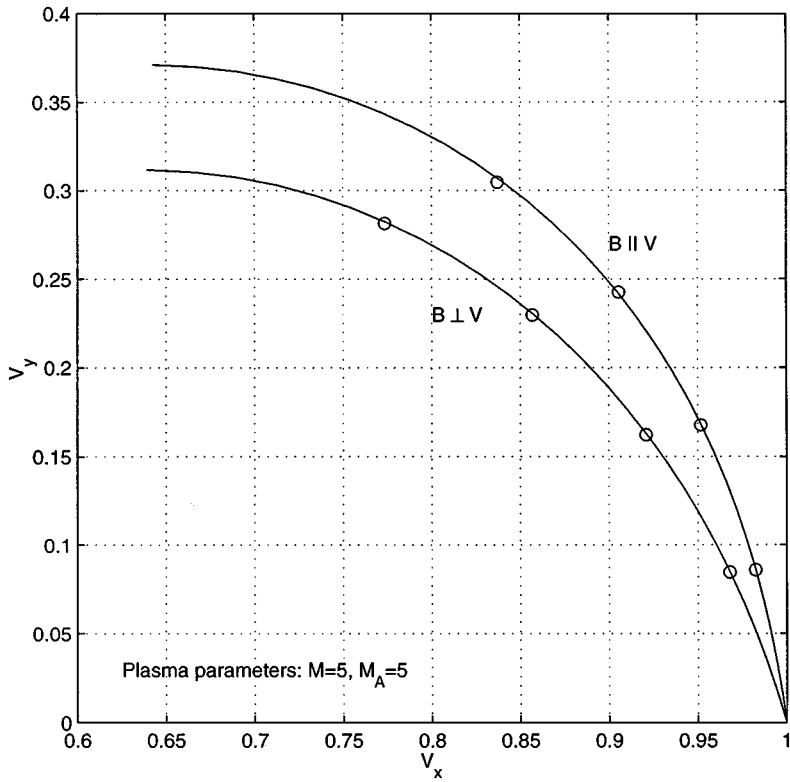
FIG. 2. Setup of oblique-shock validation case.

FIG. 3. Computed and exact shock polars.

sequence of successively finer uniform grids. Limited reconstruction was turned off, so the expectation is of first-order accuracy. Relative errors were calculated in an L_1 norm defined as

$$L_1^\eta = \frac{1}{N} \sum_{i=1}^{N} \left| \delta_i^\eta \right|,$$

where δ_i^η is the relative error in cell i of some quantity η. For example, relative errors of pressure and magnetic field magnitude are

$$\delta_i^p = \frac{p_i - p_{exact}}{p_{exact}} \tag{64}$$

$$\delta_i^B = \frac{B_i - B_{exact}}{B_{exact}}. \tag{65}$$

To assess the ability of the scheme to maintain $\nabla \cdot \mathbf{B} = 0$, the relative error

$$\delta_i^{h\nabla \cdot \mathbf{B}} = \frac{\int\int_{cell\,i} B_n\, ds}{\int\int_{cell\,i} |B_n|\, ds}$$

was calculated, where B_n is the component of the magnetic field normal to a cell face, computed by averaging the values at the cell centroids to the "left" and "right" of the face
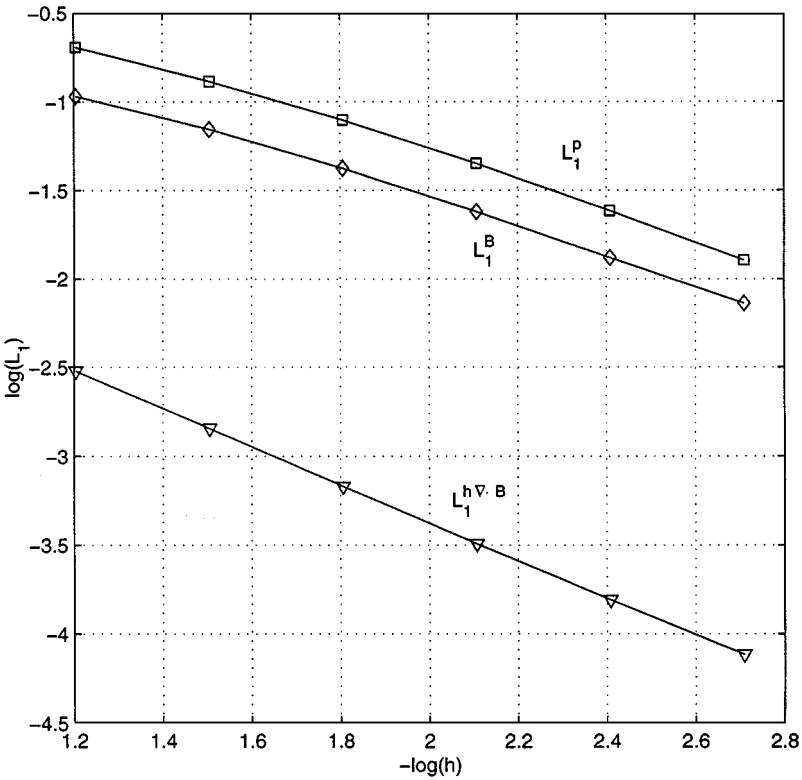
FIG. 4. Grid convergence for oblique-shock validation case.

centroid. This error is denoted as $h\nabla \cdot \mathbf{B}$ because it scales as

$$\left|\delta_i^{h\nabla \cdot \mathbf{B}}\right| \propto \frac{V|\nabla \cdot \mathbf{B}|}{A|B|},$$

where V is the cell volume and A is the cell surface area; the ratio V/A goes as the mesh spacing h.

Figure 4 shows grid-convergence results for pressure, magnetic-field magnitude, and divergence of magnetic field. The tabulated values are shown in Table I. Both the plot and the table show an imputed order of accuracy of one, as expected. In addition, it is interesting to note that the error in $h\nabla \cdot \mathbf{B}$ not only converges at the same rate as the error

TABLE I
Grid Convergence for Oblique-Shock Validation Case

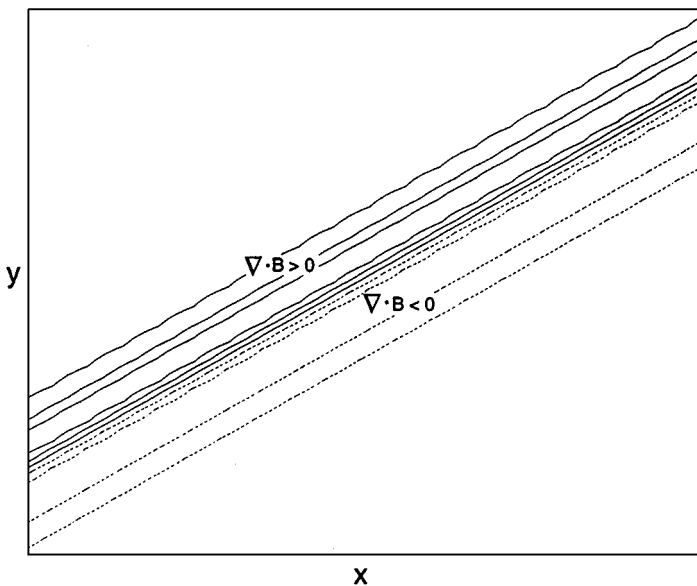| L_1^p	L_1^B	$L_1^{h\nabla \cdot \mathbf{B}}$	Resolution
0.2022690	0.1072600	0.00301172	1/16
0.130427	0.0700573	0.00143521	1/32
0.0789827	0.0422129	0.000676634	1/64
0.0449624	0.0239818	0.00032158	1/128
0.0242786	0.0131832	0.000155886	1/256
0.0127462	0.00727291	0.0000766793	1/512

FIG. 5. Structure of $\nabla \cdot \mathbf{B}$ truncation error—magnified view of a portion of a captured shock.

in other variables, it is on each grid more than an order of magnitude lower than the error in the magnetic field. The bad news here is that, since $h\nabla \cdot \mathbf{B}$ is first order, $\nabla \cdot \mathbf{B}$ itself is constant with grid refinement. However, this is, perhaps, to be expected. For any oblique discontinuity, the three terms comprising $\nabla \cdot \mathbf{B}$ will each be non-zero and of order $1/h$, and will not cancel perfectly. Since, as can be seen from examining the multi-stage scheme (Subsection 3.4), the term added in updating the conserved variables is proportional to $\Delta t \nabla \cdot \mathbf{B}$, and $\Delta t \approx h$ (from the CFL condition), comparing the $h\nabla \cdot \mathbf{B}$ term to the relative error in the magnetic field itself is appropriate.

It is also interesting to note the structure of the $\nabla \cdot \mathbf{B}$ errors. The only non-zero values are in the vicinity of the shock. Figure 5 shows contours of $\nabla \cdot \mathbf{B}$ in the vicinity of the shock; positive values are denoted by solid countrours; negative values are denoted by dashed contours. The extent of the contours of non-zero divergence is less than five cells across, typical of numerical oblique shock structures.

As can be seen, the $\nabla \cdot \mathbf{B}$ that is created numerically does not appear as isolated magnetic monopoles; any positive $\nabla \cdot \mathbf{B}$ that is created is paired with a negative contribution. This plot, and the fact that the far-field boundary conditions are divergence-free, suggest a "telescoping" property: integration of $\nabla \cdot \mathbf{B}$ over successively larger control volumes should lead to successively smaller values. Define

$$\Sigma_{\nabla \cdot \mathbf{B}} = \sum_{i=1}^{N} \left| \int \int_{control\ volume\ i} B_n\ ds \right|,$$

where N is the number of control volumes into which the grid is divided. This telescoping property can be studied by taking succesively larger control volumes for the same solution. In Table II the quantity $\Sigma_{\nabla \cdot \mathbf{B}}$ is reported for successively larger control volumes: level 9 corresponds to taking each cell in the grid as a control volume, level 8 to a control volume

<div align="center">

TABLE II

Telescoping of Magnetic-Field Divergence on a Set of Consecutively Coarsened Grids

</div>

Level	9	8	7	6	5	4	3	2	1
$\Sigma_{\nabla \cdot \mathbf{B}} \times 10^5$	1.670	1.569	1.220	0.846	0.543	0.373	0.234	0.028	0.011

consisting of eight control volumes from level 9, and so on up to level 1, where the control volume is the entire computational domain.

5.2. *Weber–Davis Flow*

Weber–Davis flow is a smooth solution to the ideal MHD equations approximating the solar wind in the equatorial plane of the interplanetary medium [11]. While a complete analytic solution for this flow does not exist, certain quantities, including

$$\Phi_M = \rho v_r r^2 \tag{66}$$

$$\Phi_B = B_r r^2 \tag{67}$$

are invariant. Thus, the method presented in this paper can be validated by calculating the degree to which Φ_M and Φ_B remain constant. The L_2 norms of the relative errors in Φ_B, Φ_M, and magnetic-field divergence are plotted in Fig. 6 and Table III for various levels of
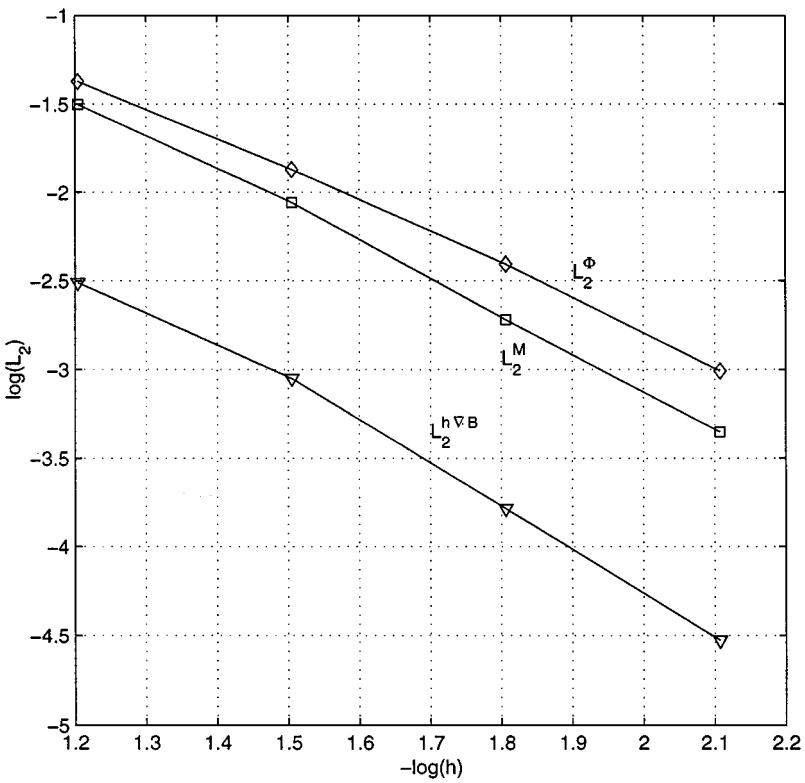
FIG. 6.   Grid convergence for Weber–Davis test case.

TABLE III
Various Levels of Grid Resolution

$L_2^{\Phi_M}$	$L_2^{\Phi_B}$	$L_2^{h\nabla \cdot \mathbf{B}}$	Resolution
0.0314475	0.042268	0.0030893	1/16
0.0087872	0.0134876	0.000889703	1/32
0.00190635	0.0039304	0.000164449	1/64
0.000444465	0.00098265	0.000029798	1/128

grid resolution; the results show second-order accuracy. Again, as in the non-smooth flow, the divergence error is more than an order of magnitude smaller than the errors in other variables.

6. SOLAR-WIND/MAGNETIZED PLANET INTERACTION RESULTS

Results are presented here for the interaction of the solar wind—a mixture of electrons, protons, helium atoms, and minor ions—with a magnetized sphere representative of Earth. This problem is a rather comprehensive test of the method described in this paper. An incoming flow that has a background magnetic field associated with it—the interplanetary magnetic field IMF—interacts with the magnetic dipole associated with Earth. The resulting flow field is a complicated balance of thermal, kinetic, and magnetic effects.

In the simulations presented here, the incoming solar wind is modeled as a 400 km/s flow with a density of 5 molecules/cm^3, an ion-acoustic speed of 50 km/s and a magnetic field strength of 10^{-8} Tesla. In the first case, the magnetic field is northward; in the second it is southward. The earth is modeled as a magnetic dipole of strength 3×10^{-5} Tesla $\times R_E^3$, where R_E is the radius of the earth. The numerical boundary conditions are free-streaming solar wind conditions on all external boundaries, and at a sphere of radius $3R_E$, the following (non-dimensional) conditions are applied

$$\rho = 1, \quad \mathbf{u} = 0, \quad B_r = 0, \quad p = 8. \tag{68}$$

A Neumann condition is applied on the other two components of the magnetic field.

Figures 7 and 8 show the converged steady-state solution for a strongly northward interplanetary magnetic field (IMF). The magnetic-field vector in the free-streaming solar wolar wind is antiparallel to the terrestrial magnetic dipole moment, consequently the z-components of the dipole field lines and the IMF are parallel. Such a situation represents fairly extreme interplanetary field conditions (B_z is too large), but it demonstrates the "closed magnetosphere" solution. Figure 9 shows the thermal pressure (color code) and magnetic field lines in the North–South meridional plane. One can clearly see the "closed magnetosphere" solution. Since the z-components of dipole and interplanetary magnetic field lines are parallel, there is very little reconnection between terrestrial and IMF field lines. The reconnection is clearly limited to a topologically zero-measure region connected to the magnetic poles of the terrestrial dipole—the cusp. This can be seen quite clearly in Fig. 10, which shows a three-dimensional rendering of the last closed field lines. One can see that for strong northward IMF the magnetosphere is quite short and there is very little connection between interplanetary and terrestrial magnetic field lines. This case, and its sensitivity to numerical parameters, is discussed more fully in [33].
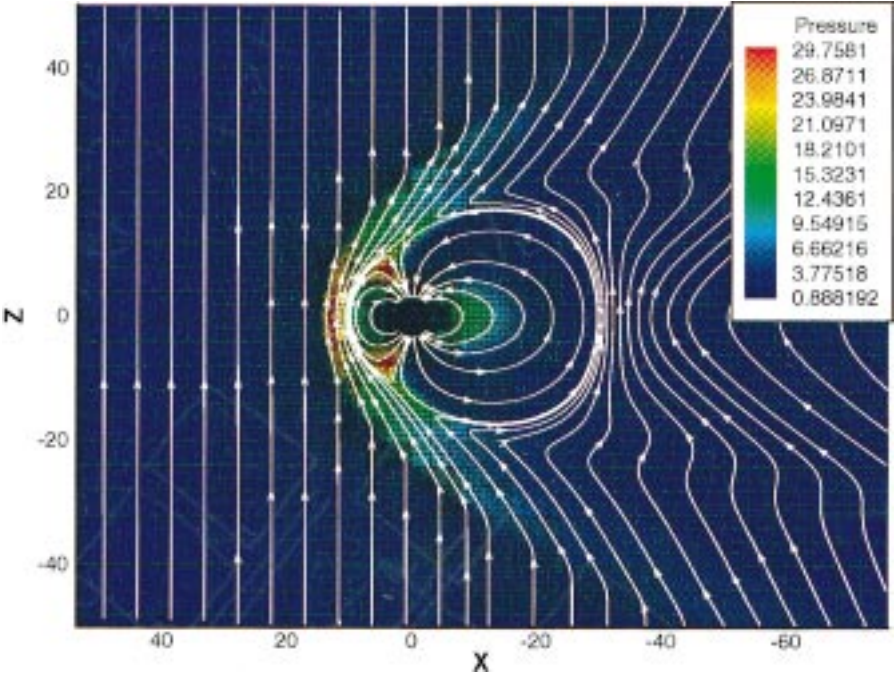
FIG. 7. Northward IMF case—pressure contours and magnetic-field lines in the north–south plane.
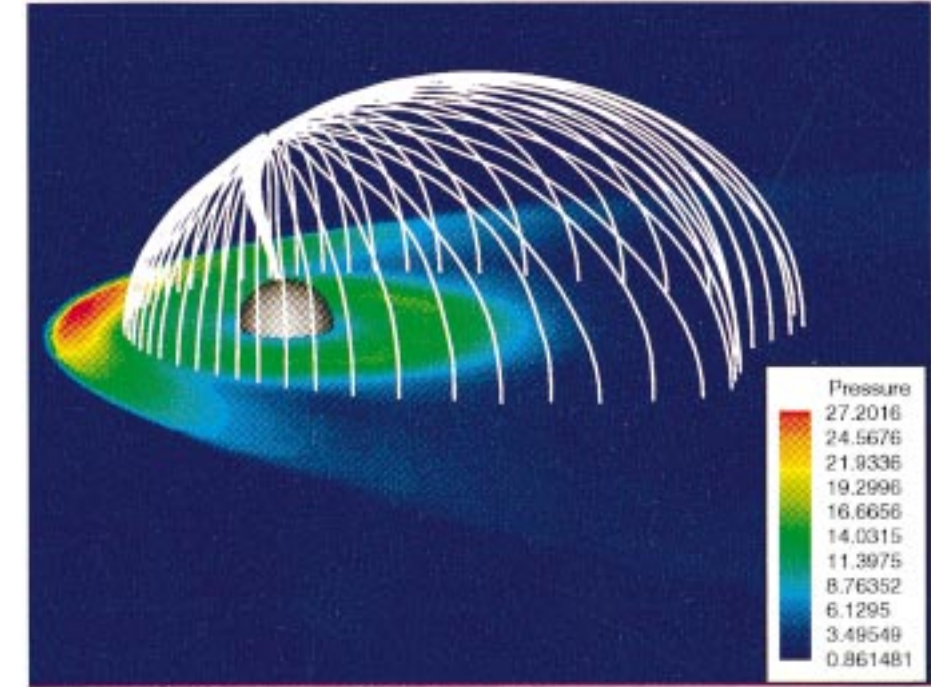
FIG. 8. Northward IMF case—pressure contours in the equatorial plane and the last closed magnetic-field lines.
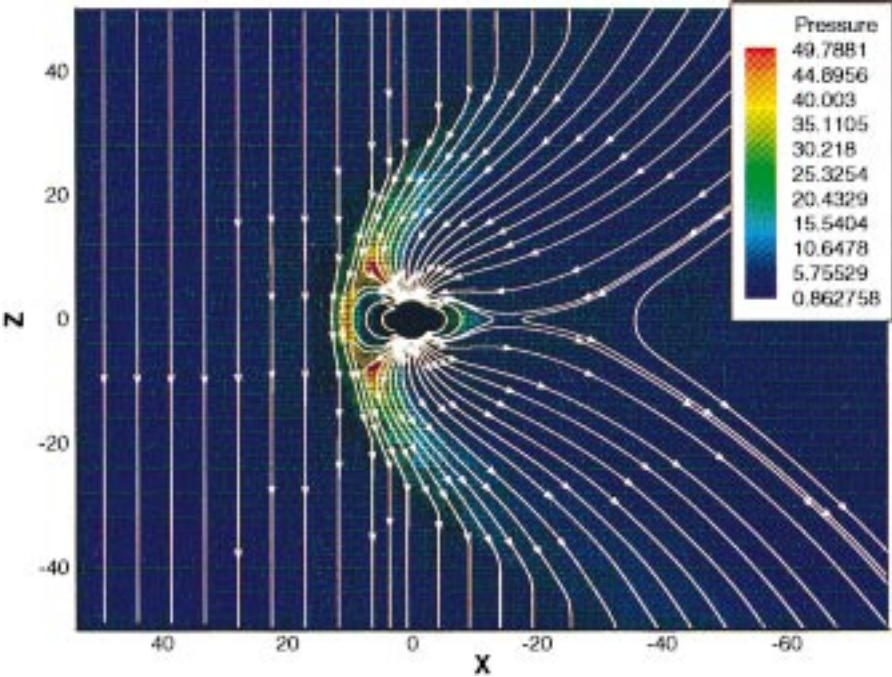
FIG. 9. Southward IMF case—pressure contours and magnetic-field lines in the north–south plane.
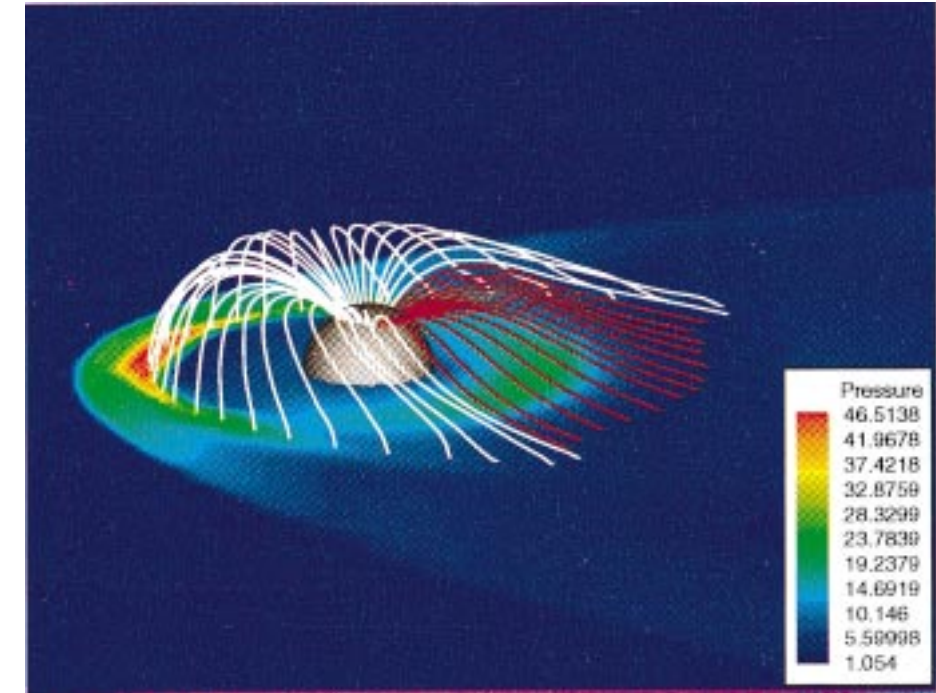
FIG. 10. Southward IMF case—pressure contours in the equatorial plane and the last closed magnetic-field lines.

Figures 9 and 10 show the results of a simulation where the solar wind parameters were identical to those in the previous simulation with the exception of the direction of the IMF, which in this case was purely southward. In these plots, field lines in red are those that end up in the tail of the magentosphere; all others are colored white. In this southward IMF case, the result is antiparallel magnetic z-components, which leads to magnetic reconnection. The topology of the magnetosphere is clearly very different from the northward IMF case. The dipole and interplanetary field lines reconnect at the dayside magnetopause and the reconnected field lines are convected downstream by the supersonic and superalfvénic solar wind plasma flow. On the nightside the field line disconnects at an X-line. This is the "open magnetosphere" configuration.

7. CONCLUDING REMARKS

A scheme for solving the compressible MHD equations in their symmetrizable form has been presented in this paper. The scheme is solution-adaptive and based on an approximate solution to the MHD Riemann problem. Grid-convergence studies were carried out on smooth and non-smooth problems, validating the accuracy of the scheme. In addition, a method for splitting off known steady magnetic fields from the solution was presented and applied in solving for the interaction of the solar wind with a magnetized planet. The combination of a robust solution method and the solution-adaptive capability yields a method that is very useful for space physics applications, which are characterized by disparate scales.

REFERENCES

1. M. Brio and C. C. Wu, An upwind differencing scheme for the equations of ideal magnetohydrodynamics, *J. Comput. Phys.* **75**, 400 (1988).

2. S. Zachary and P. Colella, A higher-order Godunov method for the equations of ideal magnetohydrodynamics, *J. Comput. Phys.* **99**, 341 (1992).

3. P. L. Roe and D. S. Balsara, Notes on the eigensystem of magnetohydrodynamics, *SIAM J. Appl. Math.* **56**(1) (1996).

4. P. R. Woodward and W. Dai, A Riemann solver for ideal magnetohydrodynamics, *J. Comput. Phys.*, in press.

5. J. Croisille, R. Khanfir, and G. Chanteur, Numerical simulation of the MHD equations by a kinetic-type method, *J. Sci. Comput.* **10**(1), 81 (1995).

6. T. Linde, *A Three-Dimensional Adaptive Multifluid MHD Model of the Heliosphere*, Ph.D. thesis, University of Michigan, 1998.

7. R. Myong, *Theoretical and Computational Investigation of Nonlinear Waves in Magnetohydrodynamics*, Ph.D. thesis, University of Michigan, 1996.

8. G. Tóth and D. Odstrcil, Comparison of some flux corrected transport and total variation diminishing numerical schemes for hydrodynamic and magnetohydrodynamic problems, *J. Comput. Phys.* **128**, 82 (1996).

9. J. U. Brackbill and D. C. Barnes, The effect of nonzero $\nabla \cdot \mathbf{B}$ on the numerical solution of the magnetohydrodynamic equations, *J. Comput. Phys.* **35**, 426 (1980).

10. J. Ramshaw, A method for enforcing the solenoidal condition on magnetic fields in numerical calculation, *J. Comput. Phys.* **52**, 592 (1983).

11. J. M. Stone, J. F. Hawley, C. R. Evans, and M. L. Norman, A test suite for magnetohydrodynamical simulations, *Ap. J.* **388**(2), 415 (1992).

12. P. R. Woodward and W. Dai, A simple finite difference scheme for multidimensional magnetohydrodynamical equations, *J. Comput. Phys.* **142**, 331 (1998).

13. S. K. Godunov, Symmetric form of the equations of magnetohydrodynamics, in *Numerical Methods for Mechanics of Continuum Medium* (1972), Vol. 1, p. 26.

14. K. G. Powell, *A Riemann Solver for Ideal MHD That Works in More Than One Dimension*, ICASE Report 94-24, 1994.

15. M. Vinokur, A rigorous derivation of the MHD equations based only on Faraday's and Ampére's laws, presentation at LANL MHD workshop, 1996.

16. W. K. Panofsky and M. Phillips, *Classical Electricity and Magnetism* (Addison–Wesley, Reading, MA), 2nd ed., Chap. 9.

17. S. K. Godunov, An interesting class of quasiliner systems, *Dokl. Akad. Nauk SSSR* **139**, 521 (1972).

18. A. Harten, High-resolution schemes for hyperbolic conservation laws, *J. Comput. Phys.* **49**, 357 (1983).

19. Q. Stout, D. De Zeeuw, T. Gombosi, C. Groth, H. Marshall, and K. Powell, Adaptive blocks: A high-performance data structure, in *Proceedings, Supercomputing '97* (1997).

20. M. J. Berger and P. Colella, Local adaptive mesh refinement for shock hydrodynamics, *J. Comput. Phys.* **82**, 67 (1989).

21. M. J. Berger, *Adaptive Finite Difference Methods in Fluid Dynamics*, Technical Report DOE/ER/0377-277, Courant Mathematics and Computing Laboratory, 1987.

22. M. J. Berger and A. Jameson, Automatic adaptive grid refinement for the Euler equations, *AIAA J.* **32**(4), 561 (1985).

23. G. Warren, W. K. Anderson, J. Thomas, and S. Krist, Grid convergence for adaptive methods, in *AIAA 10th Computational Fluid Dynamics Conference, 1991*.

24. J. J. Quirk, A parallel adaptive algorithm for computational shock hydrodynamics, *Appl. Numer. Math.*, in press.

25. T. J. Barth, On unstructured grids and solvers, in *Computational Fluid Dynamics* (Von Kármán Institute for Fluid Dynamics, 1990), Lecture Series 1990-04.

26. B. van Leer, W. T. Lee, P. L. Roe, K. G. Powell, and C. H. Tai, Design of optimally-smoothing schemes for the Euler equations, *Comm. Appl. Numer. Math.* **8**, 761 (1992).

27. B. van Leer, C. H. Tai, and K. G. Powell, Design of optimally-smoothing multi-stage schemes for the Euler equations, in *AIAA 9th Computational Fluid Dynamics Conference, 1989*.

28. T. J. Barth, Numerical methods for gasdynamic systems, in *An Introduction to Recent Developments in Theory and Numerics for Conservation Laws*, edited by D. Kröner, M. Ohlberger, and C. Rohde (Springer-Verlag, New York/Berlin, 1999).

29. P. L. Roe, Approximate Riemann solvers, parameter vectors and difference schemes, *J. Comput. Phys.* **43** (1981).

30. G. Gallice, Resolution numerique des equations de la magnetohydrodynamique ideale bidimmensionale, in *Méthodes numériques pour la MHD, 1995*.

31. A. Harten, High-resolution schemes for hyperbolic conservation laws, *J. Comput. Phys.* **49**, 357 (1983).

32. T. Tanaka, Finite volume TVD scheme on an unstructured grid system for three-dimensional MHD simulations of inhomogeneous systems including strong background potential field, *J. Comput. Phys.* **111**, 381 (1994).

33. T. I. Gombosi, D. L. DeZeeuw, C. P. T. Groth, K. G. Powell, and P. Song, The length of the magnetotail for northward IMF: Results of global 3D MHD simulations, *Phys. Space Plasmas* **15** (1998).